Colloids and Surfaces A: Physicochemical and Engineering Aspects 744 (2026) 140568

Contents lists available at ScienceDirect

Colloids and Surfaces A: Physicochemical and Engineering Aspects

journal homepage: www.elsevier.com/locate/colsurfa

Enhanced corrosion and wear resistance of 6082 Al alloy with $Al_2O_3/MoS_2/Zn_3(PO_4)_2$ MAO coatings with increased $Zn_3(PO_4)_2$

Tao Liu, Jian Shang *

School of Materials Science and Engineering, Liaoning University of Technology, Jinzhou 121001, China

HIGHLIGHTS

- A ternary composite layer comprising $Al_2O_3/MoS_2/Zn_3(PO_4)_2$ were in situ prepared by one-step MAO.
- The 12.5 g/L zinc acetate coating shows superior wear resistance in dry and corrosive environments.
- The 12.5 g/L zinc acetate coating demonstrates superior corrosion resistance in electrochemical and immersion tests.

GRAPHICAL ABSTRACT

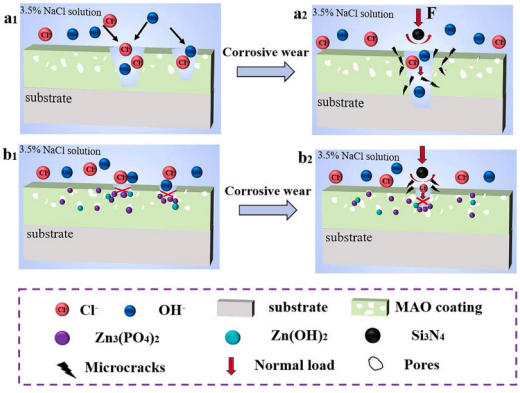

ARTICLE INFO

Keywords:
Aluminum alloy
Corrosion wear
Micro-arc oxidation
Microstructure and properties

ABSTRACT

The 6082-T6 Al alloy suffers from insufficient corrosion and wear resistance under harsh conditions, which limits its long-term service. A ternary $Al_2O_3/MoS_2/Zn_3(PO_4)_2$ composite coating was in-situ fabricated by micro-arc oxidation (MAO) in present work in order to achieve synergistic enhancement of corrosion and wear resistance via Al_2O_3, MoS_2 and Zn-containing components. The effects of zinc acetate ($C_4H_6O_4Zn$) concentration on coating microstructure, corrosion resistance, and wear performance of the MAO coatings were studied. Results indicate that zinc is enriched in the coating pores, and the porosity decreases from 3.98% to 2.55% for MZ12.5. Dry sliding and corrosive wear tests against Si_3N_4 balls show that: MZ12.5 exhibits the lowest wear rates (4.4×10^{-5} $mm^3/N{\cdot}m$ in air and 3.1×10^{-5} $mm^3/N{\cdot}m$ in 3.5 wt% NaCl solution), which are reduced by one order of magnitude compared with the MZ0, with no obvious change in the counterpart. Electrochemical tests demonstrate its corrosion current density (6.915×10^{-9} $A{\cdot}cm^{-2}$) is three orders of magnitude lower than MZ0, and a 933-hour immersion proves excellent long-term stability. In conclusion, MZ12.5 is optimal, and this MAO composite coating is a promising surface modification for 6082-T6 Al alloy in harsh environments.

* Corresponging author.
E-mail addresses: shangjian@lnut.edu.cn, shangbahao@163.com (J. Shang).

https://doi.org/10.1016/j.colsurfa.2026.140568
Received 5 February 2026; Received in revised form 12 April 2026; Accepted 15 April 2026
Available online 20 April 2026

1. Introduction

Aluminum and its alloys are widely used in the automotive, construction, marine, and aerospace industries because of their low density, high strength, and excellent processability [1–3]. A thin natural Al_2O_3 oxide coating forms on their surface, providing basic corrosion protection; however, it is thin and prone to detachment under complex service conditions (e.g., corrosive marine environments, sliding friction). The coupling of corrosion and wear accelerates material degradation, resulting in poor wear and corrosion resistance, which restricts their application range and service life [4,5]. Thus, surface modification is essential for enhancing these properties and extending their service life. Among the common techniques (anodizing, MAO, electroplating, spraying, and deposition), MAO has become a mainstream choice for aluminum alloy surface modification, offering simple processing, environmental friendliness, and high efficiency [6–8].

MAO coatings naturally possess a porous structure, which serves as a pathway for corrosive substances to penetrate, leading to localized corrosion of the substrate and hastening the failure of the coating [9–11]. To address this, researchers have made significant progress in developing various optimization strategies [12–14]. For electrical parameter regulation, a higher current density induces large discharge sparks and surface defects (pits and cracks), whereas a lower current density favors dense coatings with low roughness and porosity [15,16]. Recent studies of PEO coatings on tantalum indicate that cathodic polarization and frequency significantly affect plasma discharge characteristics and coating microstructure. The cathodic-to-anodic current density ratio (R) can regulate discharge behavior and coating properties [17–19]. Doping functional additives is a main strategy for optimizing MAO coating performance, with research advancing from single additives to multi-component synergistic systems with enhanced performance. Pezzato et al. [20,21] added recycled glass particles (LCD, borosilicate, soda-lime) to PEO electrolytes, and the pores were sealed effectively and corrosion resistance was improved (LCD glass showing optimal wear-corrosion performance). The copper-containing PEO coatings presented enhanced anti-fouling properties. Guo et al. [22] introduced graphene oxide to fabricate ultra-low porosity MAO coatings and the corrosion resistance is enhanced. For performance complementarity, multi-component synergistic strategies are widely explored. Qi et al. [23] co-added phytic acid and MoS_2 to silicate electrolytes, whose bonding and self-lubricating effects synergistically fill micropores and improve wear-corrosion resistance. Yang et al. [24] incorporated potassium fluoro-zirconate and nano-graphite into MAO electrolytes. The in-situ formed high-hardness ZrO_2 nanocrystals and self-lubricating graphite had synergistic effects to improve wear-corrosion resistance. Additionally, Zhao et al. [25] prepared CeO_2 nanoparticle-doped PEO coatings on Mg-Zn-Y-Nd alloys. The in-situ formed $CePO_4$ can seal micropores to form a dense $Mg(OH)_2/CeO_2/Ce(OH)_3$ coating, and enhance corrosion resistance and biocompatibility. Guo et al. [26] used pectin as an eco-friendly additive for MAO coatings to fill pores, inhibiting microcracks and improving corrosion resistance in simulated body fluids.

Recently, zinc-containing MAO coatings have attracted extensive attention for enhancing corrosion resistance of Al/Mg alloys. Yang et al. [27] constructed superhydrophobic double-coating coatings via "MAO coating + hydrophobically modified nanoflower shaped zinc phosphate arrays," achieving excellent corrosion resistance through physical barrier and repulsion effects. As an important corrosion-resistant phase, $Zn_3(PO_4)_2$ possesses extremely high stability in aqueous solution, with a solubility product constant Ksp $= 9.1 \times 10^{-33}$ at 298.15 K, which can effectively suppress corrosion propagation. As widely reported in organic coating systems, Cai et al. [28] doped three-dimensional multi-interface zinc phosphate particles into waterborne epoxy coatings, realizing long-term electrochemical stability and high adhesion via physical inhibition, reduced polar channels, and coordination reactions.

For present studies, much focus on binary composites, physical addition, or post-treatment methods, especially for zinc-containing MAO coatings. Few studies systematically explore the in-situ synergistic effect of $Zn_3(PO_4)_2$ with self-lubricating phases under wear-corrosion conditions. Li Qian [29] in-situ prepared $CePO_4/MoS_2/Al_2O_3$ ternary composite MAO coatings via cerium acetate and sodium molybdate addition and significantly enhance comprehensive performance through "pore filling, hardness enhancement, and lubrication synergy" effects. In present study, the green zinc source $C_4H_6O_4Zn$ and Na_2S. Na_2Mo_4 introduced into the phosphate electrolyte, and the $Al_2O_3/-MoS_2/Zn_3(PO_4)_2$ ternary composite MAO coatings successfully are fabricated in-situ on 6082-T6 alloy via a one-step method. The innovation is the integration of solid lubrication, pore filling, and passivation protection. Sodium molybdate and sodium sulfide were used to directly synthesize MoS_2 in the reaction environment. The effects of $C_4H_6O_4Zn$ concentration on the coating structure and performance were investigated, with a systematic evaluation of the tribological and corrosion resistance properties, and the relevant mechanisms were discussed.

2. Materials and methods

2.1. Materials and MAO composite coating preparation

In this study, a 6082-T6 aluminum alloy (an Al-Mg-Si alloy) with dimensions of 25 mm × 25 mm × 3 mm was used as the substrate material, whose chemical composition (wt%) is as follows: Si 1.1%, Fe 0.31%, Cu 0.05%, Mn 0.65%, Mg 0.7%, Cr 0.07%, Zn 0.07%, Ti 0.02%, and Al balance. The base electrolyte for preparing the MAO composite coating consisted of 15 g/L $(NaPO_3)_6$ + 5 g/L Na_2MoO_4 + 10 g/L Na_2S + 10 g/L EDTA. According to the concentration of $C_4H_6O_4Zn$ added to the electrolyte, the samples were designated as MZ0, MZ5, MZ7.5, MZ10, and MZ12.5, corresponding to 0, 5, 7.5, 10, and 12.5 g/L of $C_4H_6O_4Zn$, respectively. Each test experiment was done three times to establish confidence in the repeatability, and then the data were recorded.

All reagents were weighed using a precision electronic balance with an accuracy of 0.0001 g and then dissolved in a stainless-steel electrolytic cell. A beam above the cell was used to fix the electrode holder, on which a mechanical stirrer (rotating at a constant speed of 100 rpm) and alloy samples were mounted. Before the experiment, the cooling system was activated, and the electrical parameters used are presented in Table 1.

2.2. Characterization of MAO composite coatings

The thickness of the MAO composite coatings was measured from cross-sectional picture using an optical microscope. The surface hardness was determined using an automatic micro-Vickers hardness tester (2.0HV-1000Auto) under a load of 0.1 kgf and a dwell time of 10 s. Five measurements were taken for each sample, and the average was calculated. Surface roughness was evaluated using a true-color confocal microscope (HYBRID C3). The surface morphologies of the MAO composite coatings were observed using a scanning electron microscope (SEM, Zeiss Sigma 500) in secondary electron imaging mode at an accelerating voltage of 20 kV. The elemental distribution across the coating cross-section was analyzed using an energy-dispersive spectrometer (EDS, AZtec X-Max 50). The phase composition was identified by X-ray diffraction (XRD, D/max-250/pc) using a Cu/Kα target, with a voltage of 40 kV and a current of 100 mA. The scanning range was 5°–90° with a scanning speed of 8°/min. The MDI Jade 6 software with standard PDF cards was used to analyze the XRD patterns.

Wear tests were conducted in both 3.5% NaCl solution (for corrosion–wear testing) and air (for dry sliding testing) using an MS-M9000 dynamic damage and protection tester (Lanzhou Huahui Instrument Technology Co., Ltd.). A ball-on-disk configuration was adopted due to its high repeatability and good representativeness of point contact in engineering parts. With reference to the friction parameters in our study

Table 1
Electrical parameters of micro-arc oxidation.

Electric source	Operational mode	Positive/negative current density A/dm^2	Positive/negative pulse duty cycle %	Pulse frequency Hz	Duration min
AC pulse electricity	Constant current	6.5	20	500	20

[30–32,45], the experimental parameters selected are as follows: applied load of 5 N, frequency of 2 Hz, and wear length of 5 mm. which are moderate conditions commonly used to evaluate the wear resistance. A Si_3N_4 ceramic ball with a diameter of 6 mm was used as the counter ball, owing to its high hardness, chemical stability, and wide use as a counterbody for aluminum alloy components in marine and mechanical environments. The volume wear rate of the coatings was calculated using Eqs. (1–3) [33–35].

$$V = \left(\frac{2\arccos\left(\frac{\sqrt{R_1^2 - \left(\frac{S}{2}\right)^2}}{3} \right)}{360} \cdot \pi R_1^2 - \frac{T \cdot \sqrt{R_1^2 - \left(\frac{S}{2}\right)^2}}{2} \right) \cdot 2\pi R_2 \quad (1)$$

$$L = n \cdot T \quad (2)$$

$$\delta = \frac{V}{F \cdot L} \quad (3)$$

Electrochemical measurements were performed using a CHI 660E electrochemical workstation (Chenhua, Shanghai) in a standard three-electrode system, with 3.5% NaCl solution as the corrosive medium. The open-circuit potential (OCP) was monitored for 400 s. Electrochemical impedance spectroscopy (EIS) was conducted over a frequency range of 0.01 Hz to 100 kHz with an amplitude of 0.01 V. Potentiodynamic polarization curves were recorded from −1.8 to + 0.5 V vs. OCP.

3. Results and discussion

3.1. Macroscopic morphology, porosity, cross-sectional morphology, thickness, and hardness of the MAO composite coatings

Fig. 1 shows the macroscopic morphology of the prepared MAO composite coating. The coating covers the substrate surface uniformly without obvious peeling, cracks or large-area defects, presenting an intact and consistent appearance.

Fig. 2(a) displays the pore distribution morphology of the oxide coating surface at 500 × magnification, where black represents the quasi-plane and white represents micropores. The average porosities are 3.98%, 3.01%, 2.88%, 3.67%, and 2.55% for MZ0, MZ5, MZ7.5, MZ10, and MZ12.5, respectively. The porosity variation reflects the effect of $C_4H_6O_4Zn$ concentration on the surface properties. Previous studies [36, 37] reported that high porosity increases the number of micropores and discharge channels, reducing the compactness and increasing the roughness of the oxide coating, while decreasing the effective load-bearing area in hardness tests. Conversely, low porosity suggests more stable growth and a denser structure. Meanwhile, the self-sealing "circular scale" depressions become more obvious with increasing $C_4H_6O_4Zn$ concentration, which is consistent with the analysis in Fig. 3 of Section 3.2.

Figure2(b) shows the cross-sectional metallographic images of the MAO composite coatings. The left part corresponds to the 6082-T6 alloy substrate, the right part corresponds to the mounting resin, and the intermediate coating structure corresponds to the MAO ceramic coating. With increasing $C_4H_6O_4Zn$ concentration in the electrolyte, the thickness of the oxide coating generally increased. However, during the in-situ formation of the MAO coating, the growth process is often accompanied by the appearance of micropores and microcracks owing to field energy effects and the retention of reaction gases. As shown in the figure, for MZ12.5, the dense micropores in the cross-section decreased significantly, and the boundary between the dense and loose coatings [38] became indistinct. As shown in Fig. 2(c), the thickness and hardness of the MAO composite coatings exhibited a nonlinear relationship with the concentration of added $C_4H_6O_4Zn$. The oxide coating achieved a maximum hardness of 731.0 $HV_{0.1}$ for MZ5. The variations in the cross-sectional thickness, hardness, and micropore morphology of the MAO composite coatings were mainly attributed to the introduction of zinc ions into the electrolyte. Zinc participates in the micro-arc discharge process, altering the electric field distribution and discharge characteristics, which accelerates the solidification rate of molten ceramic products.

3.2. Surface morphology and roughness of the MAO composite coatings

As shown in Fig. 3(a), when the $C_4H_6O_4Zn$ concentration was 0 g/L, the micropores on the oxide coating surface exhibited a "volcanic eruption" accumulation morphology. With increasing $C_4H_6O_4Zn$ concentration, the surface pore morphology gradually transforms into a self-sealing "circular scale" structure. Three-dimensional (3D) surface topography was constructed based on selected two-dimensional (2D) regions, where green represents the quasi-plane, red represents high protrusions, and blue represents depressions. The number of 3D depressions in the selected regions increased significantly with increasing $C_4H_6O_4Zn$ concentration, confirming that the self-sealing "circular scales" are mostly distributed as depressions on the oxide coating surface.

Fig. 3(b) shows a bar chart of the surface roughness of the MAO composite coatings, where Ra is the arithmetic mean roughness and Rz

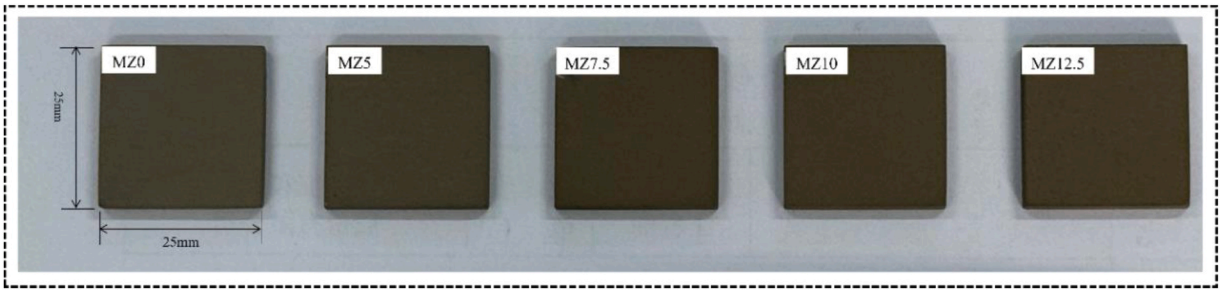

Fig. 1. Macroscopic morphology of the MAO composite coating.

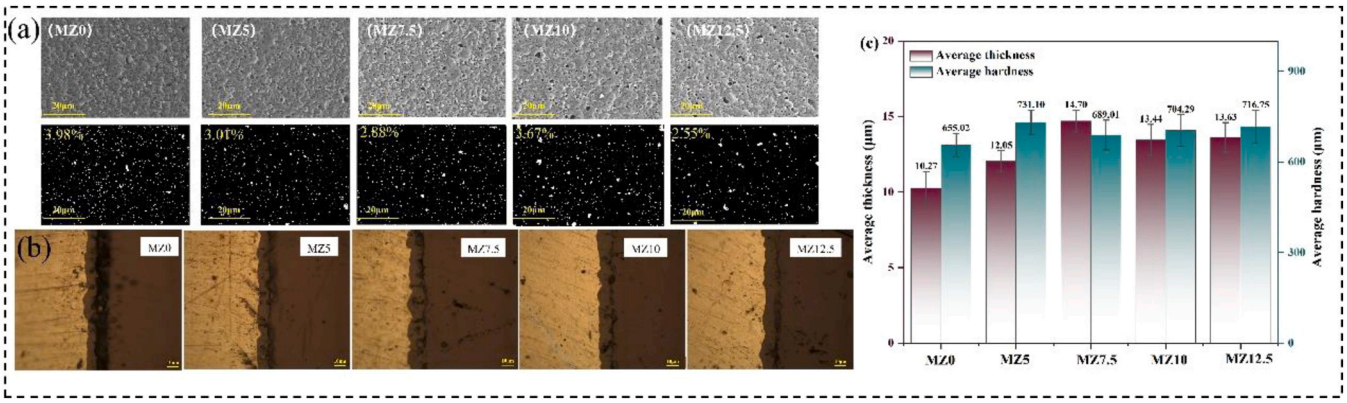

Fig. 2. (a) Porosity; (b) Cross-sectional microstructure; (c) Thickness and hardness statistics of the MAO composite coatings.

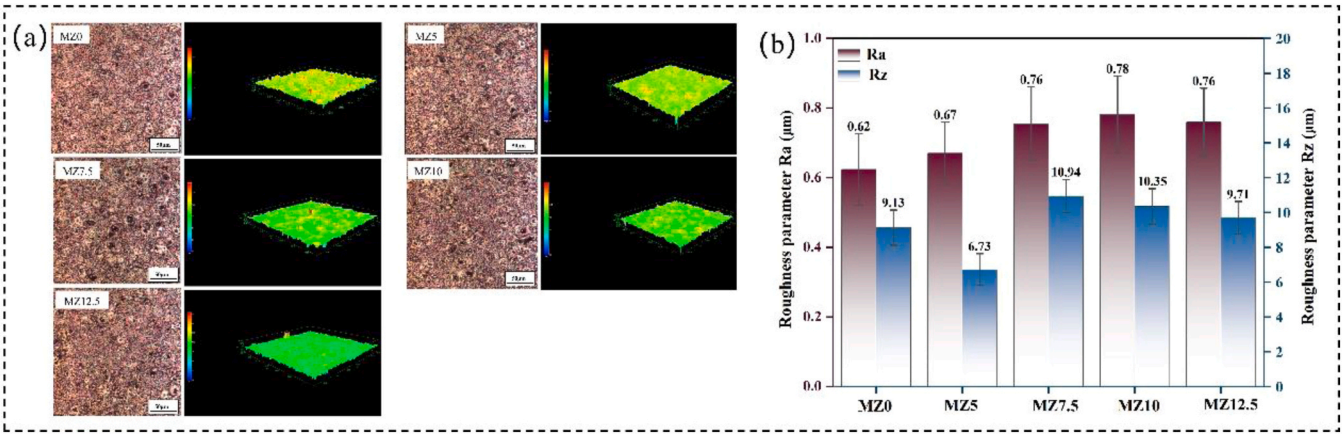

Fig. 3. (a)three-dimensional surface morphologies;(b) roughness of the composite coatings.

is the ten-point height of the micro-irregularities. The measurement results indicated that Ra ranged from 0.62 to 0.78 μm, and Rz ranged from 6.73 to 10.94 μm. Among these, Rz exhibited more significant fluctuations, which were mainly caused by changes in the $C_4H_6O_4Zn$ content during coating formation, leading to variations in the surface morphology and roughness of the oxide coating.

3.3. Phase composition and elemental distribution of the MAO composite coatings

As shown in Fig. 4(a), when the $C_4H_6O_4Zn$ concentration was 0 g/L, the phase composition of the MAO coating mainly consisted of cubic γ-Al_2O_3 (PDF# 10–0425), cubic α-Al_2O_3 (PDF# 75–0787), and a small amount of monoclinic MoS_2 (PDF# 17–0744). With increasing $C_4H_6O_4Zn$ concentration, characteristic diffraction peaks corresponding to monoclinic $Zn_3(PO_4)_2$ (PDF# 34–1490) appear at approximately $2\theta \approx 20.6^\circ$ and 21.9°, compared to the coating without $C_4H_6O_4Zn$. A distinct broadened diffuse peak emerged between these diffraction peaks, indicating the presence of an amorphous structure in the coating [39,40]. By comparing the standard diffraction peak positions in the PDF cards, this broadened peak was identified as originating from the amorphous or metastable phase of $Zn_3(PO_4)_2$. Therefore, in this MAO composite coating system, $Zn_3(PO_4)_2$ exists in a mixed state of crystalline and amorphous phases.

The elemental distribution across the cross-section of the MAO composite coatings was observed using EDS mapping, as shown in Fig. 4 (b). Aluminum and oxygen were uniformly distributed throughout the cross-section at all $C_4H_6O_4Zn$ concentrations, whereas molybdenum and sulfur were mainly concentrated in the inner region of the MAO composite coating. With increasing $C_4H_6O_4Zn$ concentration in the electrolyte, the distributions of phosphorus, Zn, Mo, and sulfur in the MAO composite coating tended to become more homogeneous. Based on the above analysis, it can be concluded that an appropriate amount of $C_4H_6O_4Zn$ can optimize the composition and structure of the oxide coating. This further confirms that the $Al_2O_3/MoS_2/Zn_3(PO_4)_2$ ternary composite MAO coating can be successfully fabricated on an aluminum substrate via a one-step self-reaction method.

3.4. Dry sliding wear behavior of the MAO composite coatings

Fig. 5(a_1) shows the dynamic friction coefficient curves for dry sliding conditions. During the initial stage (the first 6 min), the friction coefficient remained relatively stable, which was attributed to the gradual wear-in of surface asperities and the formation of a stable friction interface. As the friction time increased, the internal pores and defects were gradually exposed. Meanwhile, the wear debris generated during dry sliding cannot be effectively removed, leading to

abrasion and significant fluctuations in the friction coefficient. In addition, frictional heat may cause the surface MoS_2 to decompose into MoO_x [41,42], and local coating delamination further exacerbates the instability of the friction coefficient. Fig. 5(a_2) indicates that the MAO composite coating prepared of MZ12.5 exhibited the lowest volume wear rate (4.4×10^{-5} $mm^3/N{\cdot}m$) under dry sliding conditions, demonstrating the best wear resistance. This is attributed to the synergistic effect of the Al_2O_3-based coating and the two in-situ formed functional phases: $Zn_3(PO_4)_2$ and MoS_2. Specifically, the low porosity achieved by $Zn_3(PO_4)_2$ provides a robust load-bearing structure that prevents the lubricant from being squeezed out, while MoS_2 reduces the

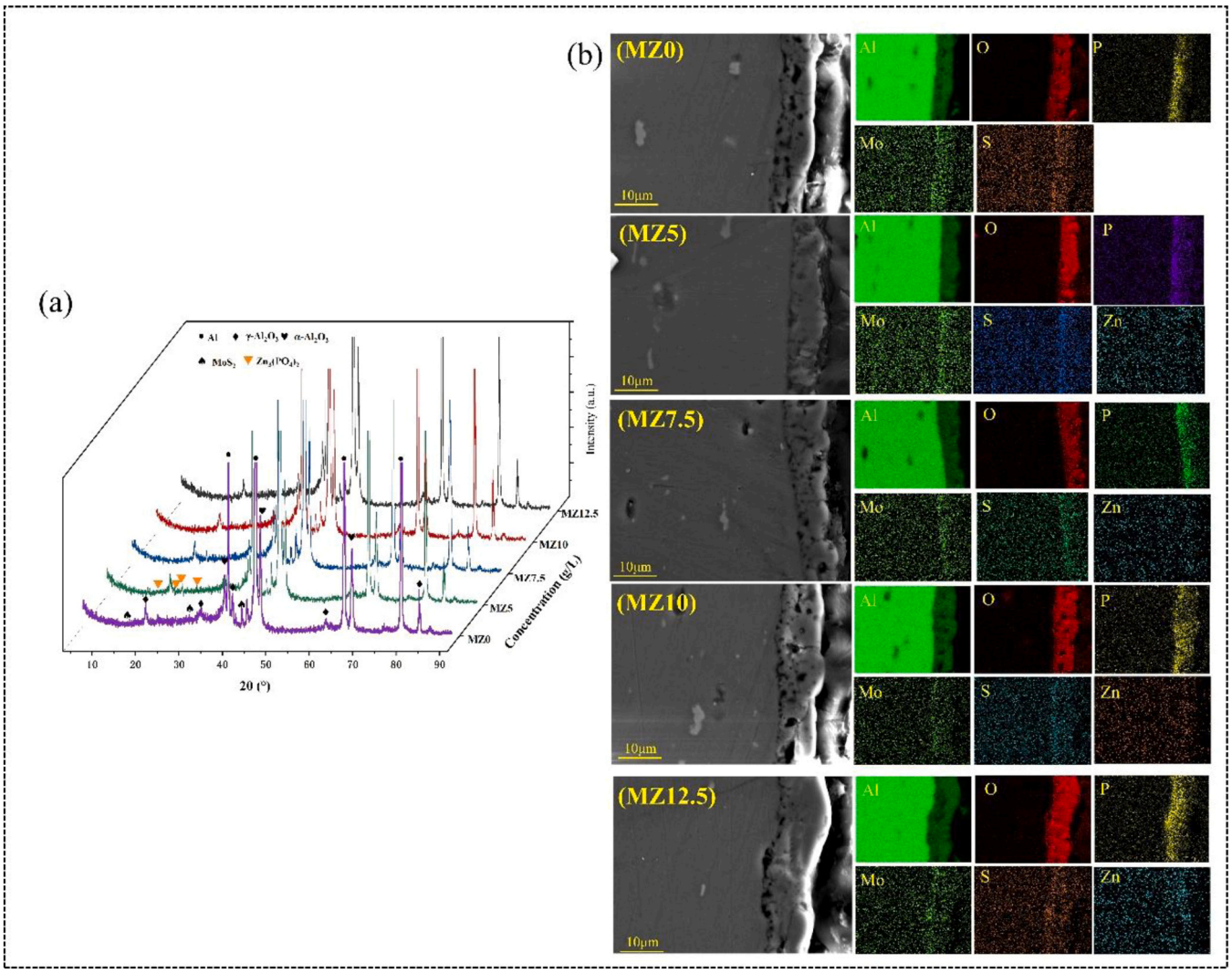

Fig. 4. (a)XRD patterns;(b) cross-sectional EDS elemental distribution maps of the MAO composite coatings.

shear stress at the interface, resulting in minimal wear.

Under dry sliding conditions, the three-dimensional wear scar morphologies and pit depths of the MAO composite coatings exhibited significantly low damage characteristics (Fig. 5(b). In this case, friction mainly arises from mechanical contact, asperity extrusion, and shear between the coating surface and counter-ball, with the dominant wear mechanisms being mild abrasive and adhesive wear. Because no corrosive medium is involved, the oxide film on the coating surface can maintain a relatively intact structure and effectively resist mechanical removal during friction. Consequently, the wear scar depths were generally small; the depth for the sample without $C_4H_6O_4Zn$ was only 16.2 μm, and it decreased to as low as 4.7 μm for MZ12.5. This stable surface state resulted in a relatively smooth wear rate of the coating during dry sliding, and the wear scar morphology also showed good uniformity without significant spalling or deep groove damage.

3.5. Corrosion behavior of the MAO composite coatings

Fig. 6 shows the potentiodynamic polarization curves of the MAO composite coating. The polarization kinetic parameters, including the corrosion current density and potential, were obtained by fitting the polarization curves using the Tafel equation. As shown in Table 2, the sample of MZ12.5 exhibited the lowest corrosion current density (6.915×10^{-9} A/cm^2), which was approximately three orders of magnitude lower than that of the sample without $C_4H_6O_4Zn$. A lower corrosion current density indicates that the corrosion rate remains relatively low, even when the material enters a corrosive state [43].

In the Nyquist plots (Fig. 7(a_1, a_2)), the capacitive loop radii decrease in the following order: MZ12.5 > MZ7.5 > MZ10 > MZ5 > MZ0. The capacitive loop radius reflects the charge transfer resistance (Rct) of the corrosion medium in solution. A larger radius indicates a higher resistance to the transfer of corrosive species, implying better corrosion resistance of the coating. The incorporation of Zn optimizes the MAO coating microstructure by reducing pore size and improving compactness, which effectively enhances the electrochemical barrier performance at the substrate interface [44]. This structural optimization inhibits the infiltration of corrosive media and suppresses the anodic dissolution of the Mg matrix, as confirmed by the higher Rct of MZ12.5.

The Bode plots show the relationship between the impedance modulus |Z| and the frequency. The low-frequency region represents the overall "resistance" of the material to current flow at different frequencies, whereas the high-frequency region is mainly related to the solution resistance (Rs). As shown in Fig. 7(b_1, b_2), the total impedance |Z| at low frequencies follows the order: MZ12.5 > MZ7.5 > MZ10 > MZ5 > MZ0. This indicates that MZ12.5 had the highest corrosion resistance. In the phase angle plots, the phase angle was relatively low at low frequencies, exhibiting resistive behavior. As the frequency increased, the phase angle gradually increased, indicating an enhancement in the capacitive behavior. As shown in Fig. 7(c), the phase angle curves for all concentrations show an

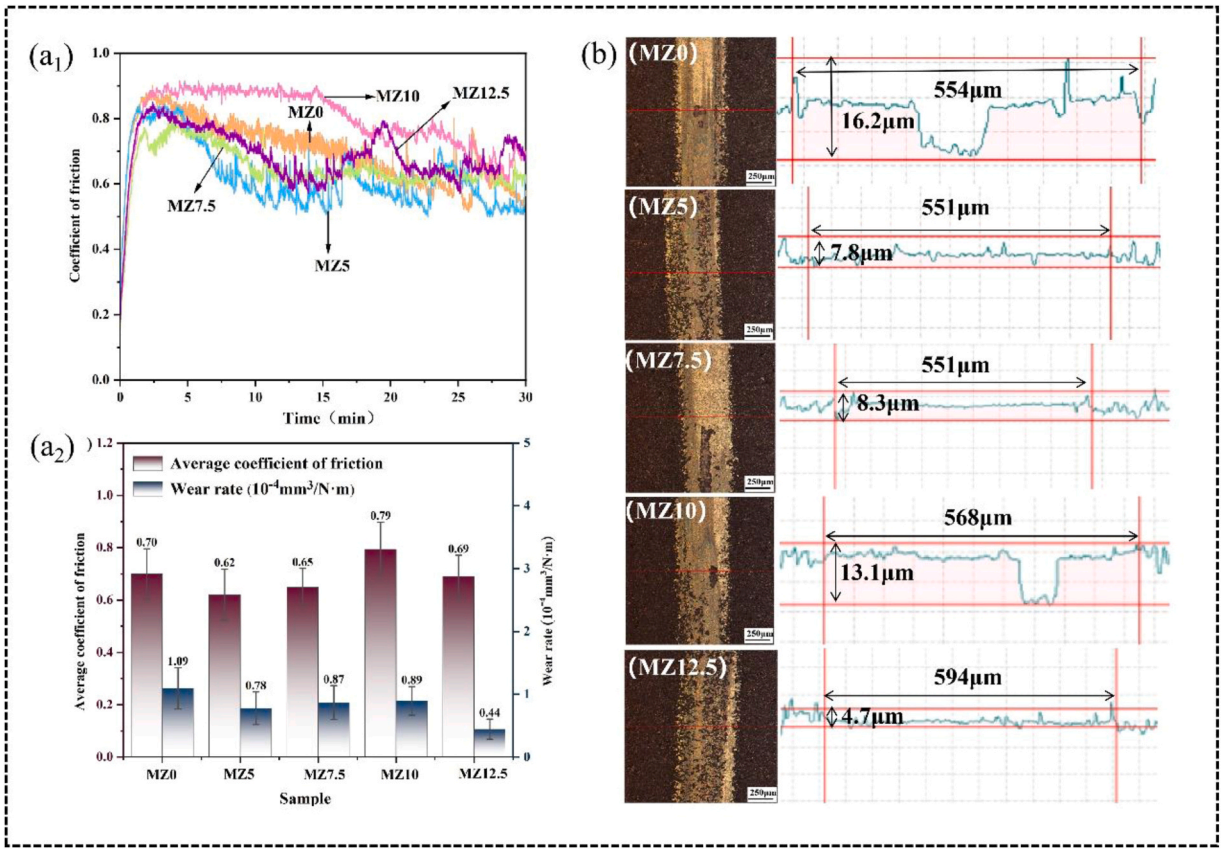

Fig. 5. Friction properties of the MAO composite coatings under dry sliding conditions: (a_1) Dynamic friction curves; (a_2) Average friction coefficient and wear rate; (b) Three-dimensional morphology of the worn track.

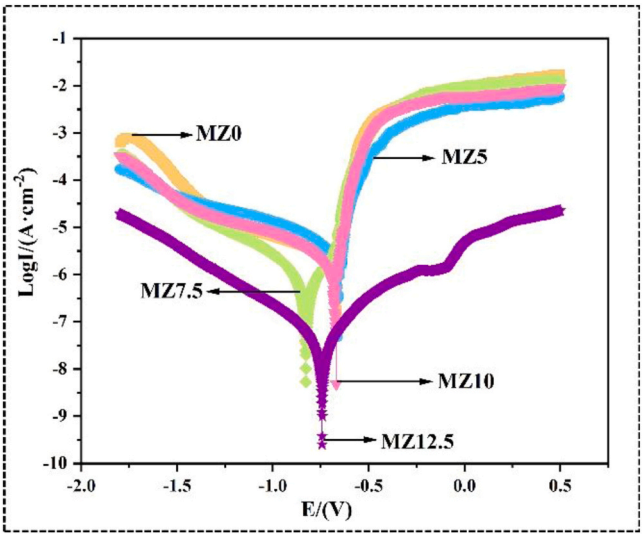

Fig. 6. Potentiodynamic polarization curves of the MAO composite coatings in 3.5% NaCl solution.

increasing trend. Among them, MZ12.5 exhibits the highest phase angle and the broadest frequency range corresponding to the peak phase angle, which is closely related to the capacitive behavior and charge transfer resistance of the coating. A higher and broader phase angle peak usually indicates a more uniform interface structure of the coating. Uniform distribution of Zn can fill micro-defects and reduce interface inhomogeneity. This characteristic phase angle response over a wide frequency range is a typical sign of excellent anticorrosive performance,

Table 2
Electrochemical corrosion parameters of the MAO composite coatings obtained from potentiodynamic polarization curves.

Sample	Ecorr (V)	Icorr (A·cm^{-2})
MZ0	-0.692	1.696×10^{-6}
MZ5	-0.631	1.544×10^{-6}
MZ7.5	-0.828	2.418×10^{-7}
MZ10	-0.672	9.772×10^{-7}
MZ12.5	-0.727	6.915×10^{-9}

consistent with the barrier mechanism of functional filler-modified coatings [45].

Comparing MZ12.5 and MZ0, the imaginary part of the impedance (Z″) in the Nyquist plot increased by two orders of magnitude, the total charge transfer resistance |Z| in the Bode plot increased by three orders of magnitude, and the capacitive effect in the phase-angle plot was significantly enhanced in the medium-to-high frequency range. Combined with the fitted equivalent circuit (Fig. 7(d)) and the equivalent resistance values in Table 3, it can be concluded that MZ12.5 exhibited the best corrosion resistance.

Table 4 shows the changes in Zn content within the pores of the MAO composite coatings before and after immersion in 3.5% NaCl solution. It can be observed that the Zn content in the coating before immersion gradually increases with the increase of zinc acetate concentration, which confirms that Zn is successfully incorporated into the MAO coating during the preparation process. Microscopic observation and elemental scanning of the MAO composite coating surface using scanning electron microscopy confirmed the presence of Zn within the pores of the coating. It can be seen that the Zn content of all samples after immersion is lower than that before immersion, indicating that Zn

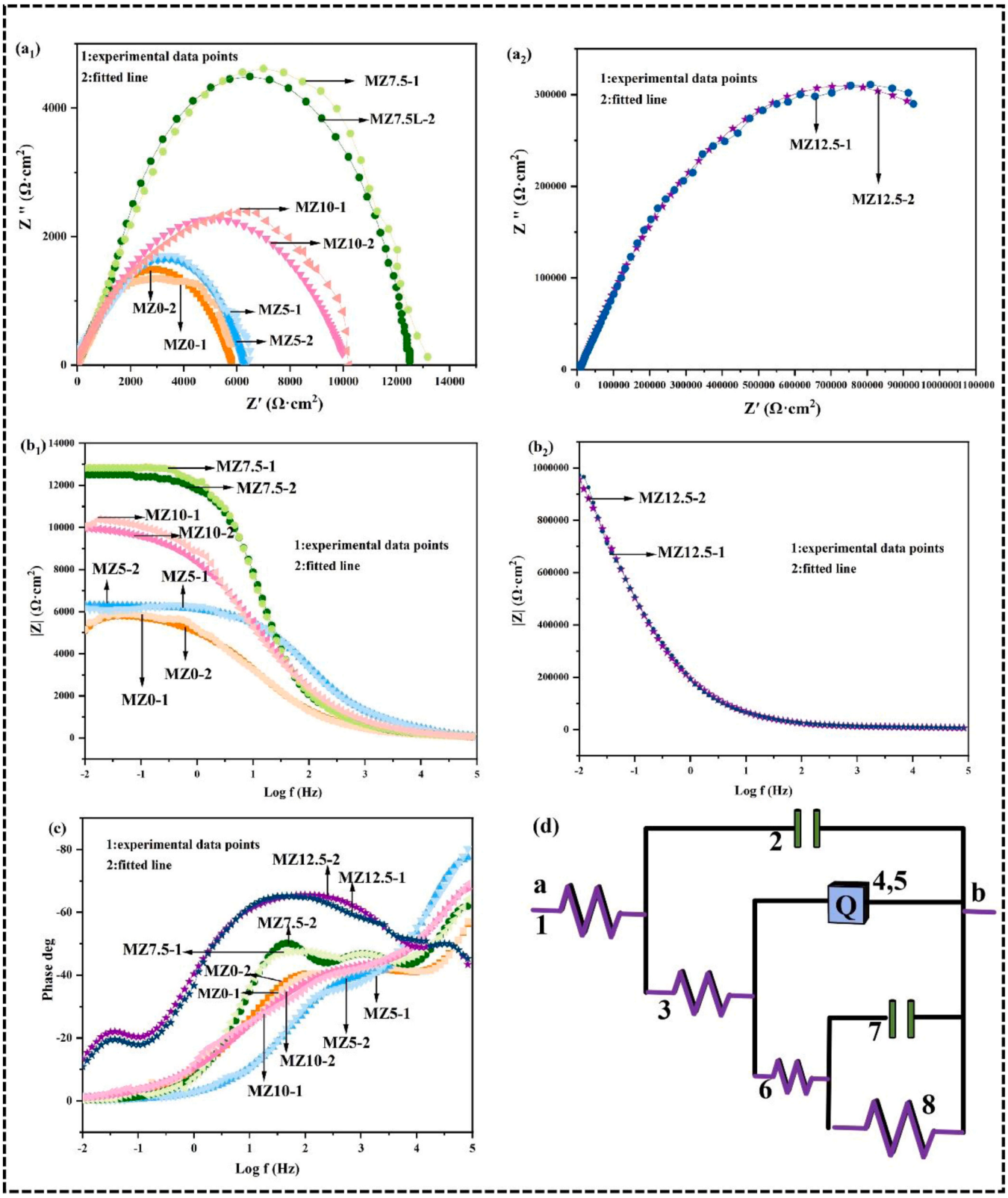

Fig. 7. (a_1, a_2) Nyquist plots; (b_1, b_2) Bode magnitude plots; (c) Bode phase-angle plots; (d) Equivalent circuit model used for fitting the EIS data.

dissolved during corrosion and participated in the formation of corrosion products. Among them, MZ12.5 retained the highest Zn content after immersion, which was significantly higher than the MZ5, MZ7.5, and MZ10 groups, suggesting that the dissolution loss of Zn was minimal at this concentration. The mass difference results shown in Fig. 8 further support this conclusion. MZ12.5 exhibited the lowest mass loss, indicating the least material loss during corrosion and the most stable coating structure. Combined with Table 2 and Fig. 8, it can be inferred that the higher Zn retention rate in MZ12.5 contributed to the formation of a stable corrosion product film, thereby reducing further dissolution

Table 3
Fitted equivalent circuit parameters of the MAO composite coatings.

Sample		MZ0	MZ5	MZ7.5	MZ10	MZ12.5
1	R	1.099×10^{-3}	7.422×10^{-3}	1.435×10^{-2}	5.743×10^{-3}	7.01×10^{-3}
2	C	2.262×10^{-8}	2.269×10^{-8}	3.317×10^{-8}	2.891×10^{-8}	2.204×10^{-10}
3	R	1.865×10^{4}	1.986×10^{4}	4.009×10^{5}	1.9×10^{5}	3.665×10^{5}
4	Q-Yo	1.434×10^{-5}	3.449×10^{-6}	2.604×10^{-6}	1.114×10^{-5}	1.870×10^{-6}
5	Q-n	0.678	0.737	0.825	0.539	0.816
6	R	3.028×10^{5}	5.706×10^{5}	8.834×10^{5}	9.936×10^{5}	1.443×10^{6}
7	C	8.938×10^{-1}	6.661×10^{-7}	6.956×10^{-9}	2.635×10^{-9}	9.742×10^{-11}
8	R	4.745×10^{4}	2.745×10^{5}	1.502×10^{6}	2.044×10^{5}	2.826×10^{6}
	χ^2	2.136×10^{-3}	3.223×10^{-3}	5.668×10^{-3}	5.623×10^{-3}	6.372×10^{-3}

Table 4
Zn content changes in the pores of MAO composite coatings before and after immersion in 3.5% NaCl solution.

Sample	Microscopic morphology before immersion	Zn content	Microscopic morphology after immersion	Zn content
MZ5	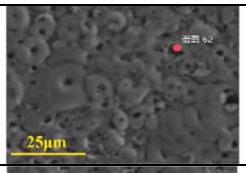	5.53%	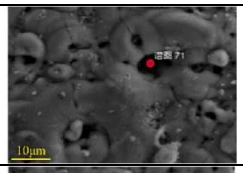	3.50%
MZ7.5	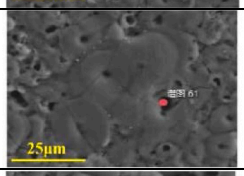	37.45%		18.63%
MZ10	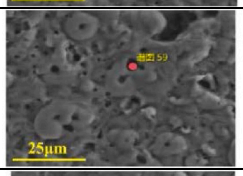	44.67%	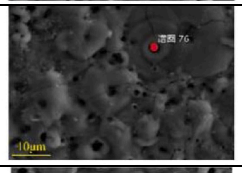	20.85%
MZ12.5	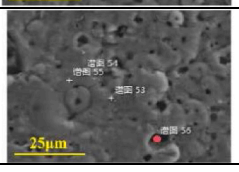	49.09%	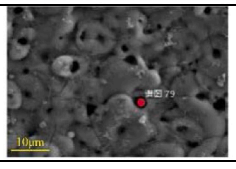	33.27%

and material loss.

In summary, the Zn retention rate showed a good correlation with the mass loss of the samples, and MZ12.5 exhibited the best structural stability and resistance to corrosion-induced dissolution.

3.6. Corrosive wear behavior of the MAO composite coatings

Fig. 9(a_1) shows the dynamic friction coefficient curves of the MAO composite coatings in a 3.5% NaCl solution. In the initial stage of the corrosion–wear coupling (the first 2.5 min), the friction coefficient changes steeply with time, which is attributed to the initial contact and running-in between the counter-ball and surface asperities or hard particles of the MAO composite coating. Among all groups, MZ5 acetate sample exhibited the smallest fluctuation in the friction coefficient, indicating the best initial stability. After 5 min of wear, the fluctuation of the friction coefficient decreased significantly and entered a stable stage. The stable friction coefficients for MZ0, MZ5, MZ7.5, MZ10, and MZ12.5 were 0.33, 0.25, 0.28, 0.27, and 0.26, respectively, all of which were low and stable.

Fig. 9(a_2) shows that MZ12.5 exhibited the lowest volume wear rate of 3.1×10^{-5} mm^3/N·m, which is one order of magnitude lower than those of the other concentration groups. This superior performance is attributed to the synergistic effect of the dense $Zn_3(PO_4)_2$-filled structure and the in-situ formed MoS_2 lubricant.

Under corrosive conditions, the wear morphology of the MAO composite coatings differed significantly from those under dry sliding, with much deeper wear scars and more complex damage mechanisms (Fig. 9(b)). The presence of a corrosive medium induces a synergistic effect between electrochemical corrosion and mechanical wear. On one hand, the corrosive medium continuously attacks the coating surface and internal defects, dissolving the oxide film and destroying the structural integrity of the coating. On the other hand, the mechanical forces during friction accelerate the spalling of corrosion products and expose fresh substrate surfaces, which provide more active sites for subsequent corrosion reactions. This “corrosion–wear” cyclic effect significantly accelerates surface damage, resulting in much deeper wear scars than those observed under dry sliding conditions. In the absence of $C_4H_6O_4Zn$, the coating lacked effective corrosion-resistant components, and the surface oxide film was prone to cracking and spalling in the corrosive medium, leading to a maximum wear scar depth of 61.3 μm and a sharp decline in wear resistance. With the addition of $C_4H_6O_4Zn$, zinc ions participate in the film-forming process and form $Zn_3(PO_4)_2$

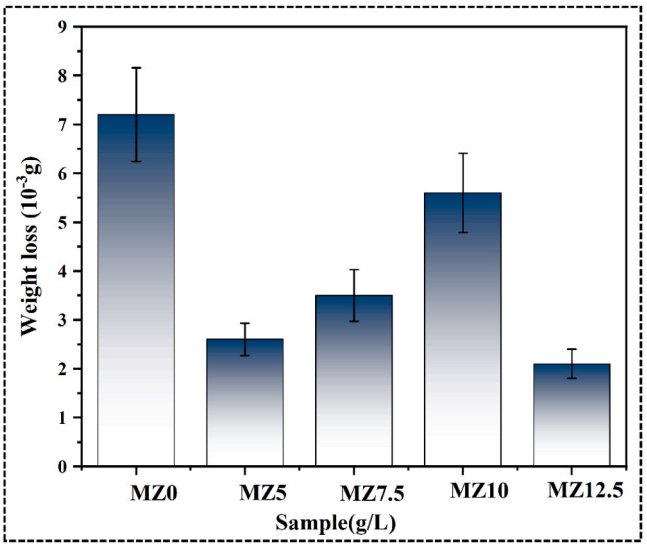

Fig. 8. Weight loss of the MAO composite coatings before and after 933 h immersion in 3.5 wt% NaCl solution.

phases, which can fill the coating pores and block the penetration paths of the corrosive medium, thereby effectively suppressing the synergistic effect of corrosion and wear. For MZ12.5, the wear scar depth decreased sharply, significantly improving the damage resistance of the MAO composite coating under corrosive conditions [46,47].

4. Corrosion and wear mechanisms of the MAO composite coatings

In this study, an $Al_2O_3/MoS_2/Zn_3(PO_4)_2$ ternary MAO composite coating was successfully prepared on a 6082-T6 aluminum alloy, which effectively improved its wear and corrosion resistance. The corrosion mechanism is illustrated schematically in Fig. 10.

In the MAO composite coating without $C_4H_6O_4Zn$ (Fig. 10a$_1$), the main component was Al_2O_3. Although this phase exhibits a certain degree of corrosion resistance, the porous structure of the MAO coating allows Cl^- ions to penetrate the coating and attack the substrate under long-term corrosion [48,49], leading to the anodic dissolution of aluminum, as shown in Eq. (4):

$$Al \rightarrow Al^{3+} + 3e^- \quad (4)$$

Meanwhile, cathodic reactions, including oxygen reduction and hydrogen evolution (Eq. 5 and 6), generate a high concentration of OH^- at the interface of the electrode. Al^{3+} initially reacts with OH^- to form $Al(OH)_3$ (Eq. 7), However, this product is unstable in NaCl solution and readily transforms into porous and loose $Al(OH)_{3-n}Cl_n$ (Eq. 8) [50]. This porous corrosion product cannot provide effective barrier protection, resulting in continuous pitting corrosion and eventual coating failure.

$$O_2 + 2H_2O + 4e^- \rightarrow 4OH^- \quad (5)$$

$$2H_2O + 2e^- \rightarrow H_2 + 2OH^- \quad (6)$$

$$Al^{3+} + 3OH^- \rightarrow Al(OH)_3 \quad (7)$$

$$Al(OH)_3 + nCl^- \rightarrow Al(OH)_{3-n}Cl_n + nOH^- (n = 1, 2, 3) \quad (8)$$

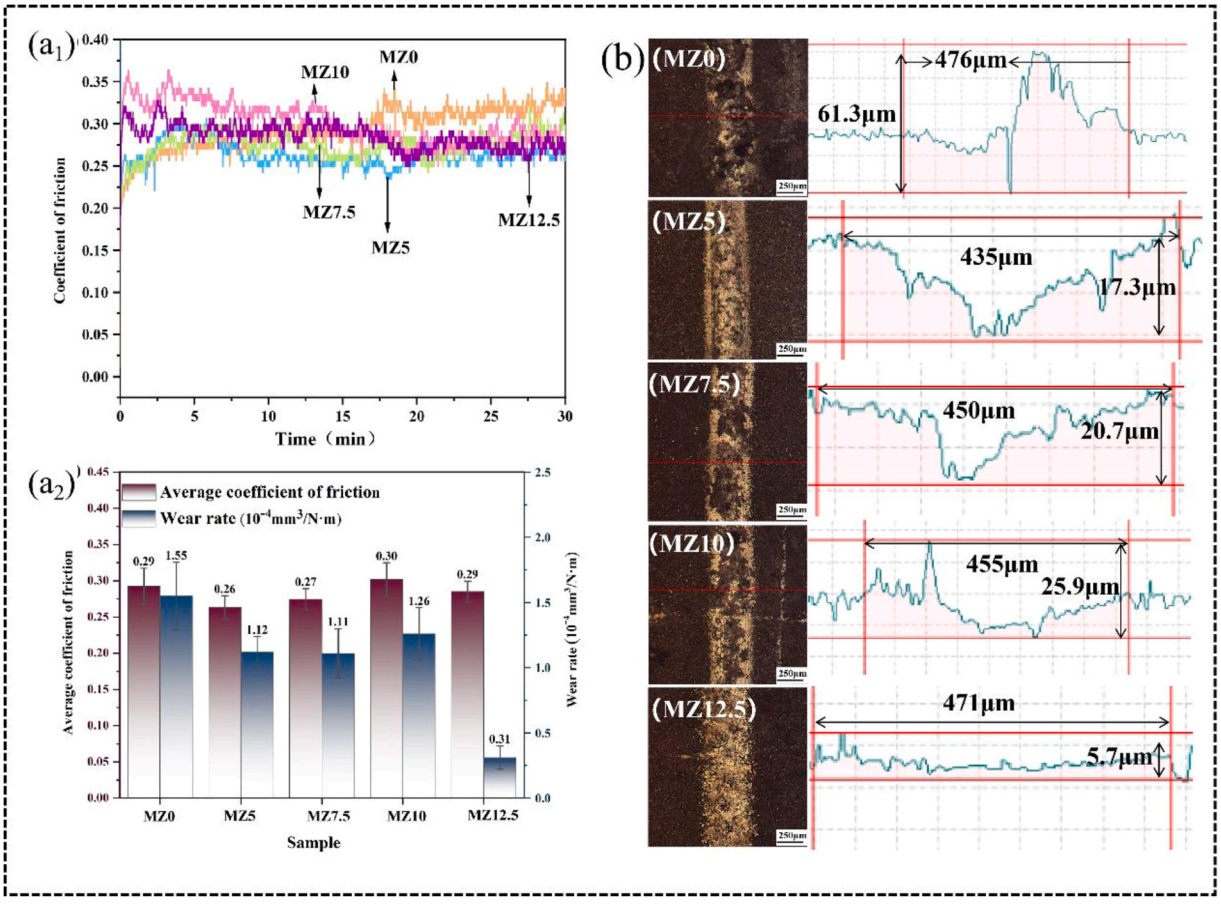

Fig. 9. Friction properties of the MAO composite coatings under corrosive conditions: (a$_1$) Dynamic friction curves; (a$_2$) Average friction coefficient and wear rate; (b) Three-dimensional morphology of the worn track.

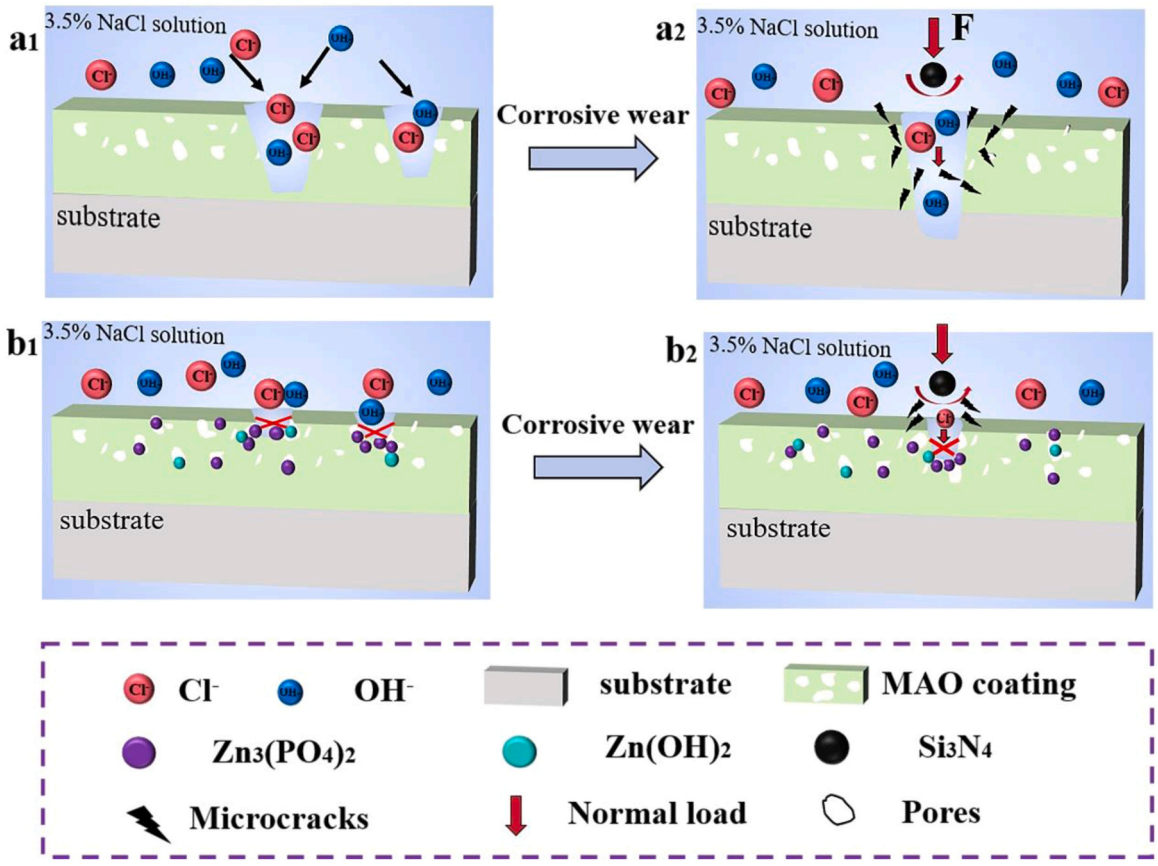

Fig. 10. Corrosion and wear mechanisms of MAO composite coatings:(a_1, a_2) Without $C_4H_6O_4$ Zn addition: (a_1) wear mechanism, (a_2) corrosion mechanism;(b_1, b_2) With $C_4H_6O_4$n addition: (b_1) wear mechanism, (b_2) corrosion mechanism.

In contrast, the addition of $C_4H_6O_4Zn$ fundamentally altered the corrosion mechanism (Fig. 10(b_1、b_2)). During the MAO process, $C_4H_6O_4Zn$ first undergoes thermal decomposition at the high temperature of the discharge channels to form zinc oxide. As the temperature increases further, ZnO vaporizes and ionizes in the plasma environment, generating reactive zinc ions (Eqs. 9 and 10):

$$Zn(CH_3COO)_2 \rightarrow ZnO + 2CO_2 + 2CH_4 \quad (9)$$

$$ZnO \rightarrow Zn^{2+}O^{2-} \quad (10)$$

Simultaneously, sodium hexametaphosphate undergoes high-temperature depolymerization to form orthophosphate ions (PO_4^{3-}), as shown in Eq. 11:

$$(NaPO_3)_6 + 3O^{2-} \rightarrow 6Na^{+} + 6PO_4^{3-} \quad (11)$$

These ions react within the molten alumina matrix and eventually form zinc phosphate in situ (Eq. 12). $Zn_3(PO_4)_2$ was uniformly distributed in the Al_2O_3 matrix and preferentially accumulated in the pores, acting as a fundamental physical barrier that hindered the initial intrusion of Cl^- ions.

$$3Zn^{2+} + 2PO_4^{3-} \rightarrow Zn_3(PO_4)_2 \quad (12)$$

$$Zn_3(PO_4)_2 \rightarrow 3Zn^{2+} + 2PO_4^{3-} \quad (13)$$

$$Zn^{2+}2OH^{-} \rightarrow Zn(OH)_2 \quad (14)$$

Furthermore, when localized corrosion occurs, $Zn_3(PO_4)_2$ reacts with the NaCl solution, gradually dissolving and releasing Zn^{2+} ions, which subsequently react with OH^- to form dense Zn $(OH)_2$ (Eqs. 13 and 14) [51]. This dynamic "dissolution–deposition" process effectively seals micropores and blocks the transport of corrosive media, thereby endowing the coating with excellent self-healing ability.

5. Conclusion

In this study, an $Al_2O_3/MoS_2/Zn_3(PO_4)_2$ ternary composite layer was fabricated in situ on 6082-T6 aluminum alloy by a one-step MAO method. The microstructure, phase composition, wear and corrosion resistance were systematically investigated. The in-situ formation of MoS_2 and $Zn_3(PO_4)_2$ is contributed to improve their mechanical, wear and corrosion resistance.

$C_4H_6O_4Zn$ acts as a zinc source, reacting with phosphate ions to form $Zn_3(PO_4)_2$ that preferentially fills the coating's pores and defects—a key improvement over conventional unfilled MAO coatings. The addition of $C_4H_6O_4Zn$ enhances mechanical properties: maximum hardness (731.10 $HV_{0.1}$) is achieved at MZ5, while for MZ12.5, porosity decreases to 2.55% (36% lower than the MZ0). Wear tests show the MAO composite coatings exhibit remarkable friction reduction and reduced wear rates under dry sliding and 3.5% NaCl conditions. The MZ12.5 has the lowest volume wear rates (3.1×10^{-5} $mm^3/(N{\cdot}m)$) in NaCl, 4.4×10^{-5} $mm^3/(N{\cdot}m)$ under dry sliding), outperforming many reported MAO-based coatings. Electrochemical and 933 h immersion tests confirm enhanced corrosion resistance: MZ12.5's self-corrosion current density is three orders of magnitude lower than MZ0, with the lowest mass and Zn element loss rates—evidencing excellent long-term service stability for engineering applications. The optimal sample is MZ12.5, attributed to synergistic effects: $Zn_3(PO_4)_2$ fills pores and forms a self-healing Zn $(OH)_2$ film, while $Zn_3(PO_4)_2$ and MoS_2 exert joint lubrication.

This study provides a one-step strategy for high-performance MAO composite coatings and offers guidance for designing protective layers" to

summarize the academic contribution of this work, and added "Future work will focus on optimizing MAO parameters, improving layer-substrate bonding, exploring applications in corrosive wear environments.

CRediT authorship contribution statement

Tao Liu: Writing – original draft, Investigation, Formal analysis, Data curation. **Shang jian:** Writing – review & editing, Supervision, Funding acquisition.

Declaration of Competing Interest

The authors declare the following financial interests/personal relationships which may be considered as potential competing interests: Jian Shang reports equipment, drugs, or supplies was provided by Liao Ning Revitalization Talents Program. If there are other authors, they declare that they have no known competing financial interests or personal relationships that could have appeared to influence the work reported in this paper

Acknowledgement

This work is funded by Liao Ning Revitalization Talents Program (XLYC2403197).

Data availability

Data will be made available on request.

References

[1] Z. Guo, J. Song, G. Wang, G. Zhao, Enhancing the tribological and corrosion properties of 2A12 aluminum alloy via micro-arc oxidation and paraffin sealing, COLLOID Surf. A (2025) 136476, https://doi.org/10.1016/j.colsurfa.2025.136476.
[2] D.L. Yu, B. Jiang, X. Qi, C. Wang, R.G. Song, Study on the microstructure and comprehensive properties of black MAO/TiO2 coatings prepared on 6063 aluminum alloy, Mater. Today Commun. 42 (2025) 111317, https://doi.org/10.1016/j.mtcomm.2024.111317Get (rights and content).
[3] A. Abd El-Aty, Y. Xu, X. Guo, S.-H. Zhang, Y. Ma, D. Chen, Strengthening mechanisms, deformation behavior, and anisotropic mechanical properties of Al-Li alloys: a review, J. Adv. Res. 10 (2018) 49–67, https://doi.org/10.1016/j.jare.2017.12.004.
[4] G.P. Zhao, Y.H. Yuan, P. Zhang, C.L. Zang, J.L. Zhang, L.X. Tao, G.H. Zhang, H. Zhou, Effects of laser-processed unit distribution density on wear resistance of biomimetic 6082 aluminum alloy, Opt. Laser Technol. 112 (2019) 175–182, https://doi.org/10.1016/j.optlastec.2018.11.021.
[5] W.J. Liang, P.A. Rometsch, L.F. Cao, N. Birbilis, General aspects related to the corrosion of 6xxx series aluminium alloys: exploring the influence of Mg/Si ratio and Cu, Corros. Sci. 76 (2013) 119–128, https://doi.org/10.1016/j.corsci.2013.06.035.
[6] H. Fan, L. Yang, D. Zhang, et al., Enhancing epoxy coating corrosion resistance with a novel MoS2-modified polydopamine functionalized graphene oxide nanocomposite, COLLOID Surf. A 683 (2024) 133080, https://doi.org/10.1016/j.colsurfa.2023.133080.
[7] R. Gabor, M. Doubkova, L. Cvrcek, et al., Enhancing early osteogenic differentiation on Ti6Al4V implants via MAO coatings doped with strontium and calcium, COLLOID Surf. A (2025) 139438, https://doi.org/10.1016/j.colsurfa.2025.139438.
[8] J.Z. Tang, F. Wei, L. Zhao, L. Yang, J. Li, Z.Q. Sun, C.G. Yang, W.Q. Zhang, B.D. Liu, Superior antibacterial properties of copper-doped titanium oxide films prepared by micro-arc oxidation, Ceram. Int. 50 (2024) 1370–1378, https://doi.org/10.1016/j.ceramint.2023.10.225.
[9] K. Xi, H. Wu, C.L. Zhou, Z.Y. Qi, K.L. Yang, R.K.Y. Fu, S. Xiao, G.S. Wu, K.J. Ding, G.H. Chen, P.K. Chu, Improved corrosion and wear resistance of micro-arc oxidation coatings on the 2024 aluminum alloy by incorporation of quasi-two-dimensional sericite microplates, Appl. Surf. Sci. 585 (2022) 152693, https://doi.org/10.1016/j.apsusc.2022.152693.
[10] H.C. Li, H.J. Yu, C.Z. Chen, W.X. Zhong, Effect of graphene oxide on corrosion resistance and biological activity of micro arc oxidation ceramic coating on titanium alloy, Mater. Lett. 327 (2022) 133056, https://doi.org/10.1016/j.matlet.2022.133056.
[11] L.X. Chen, Y.Y. Sheng, H.Y. Zhou, Z.B. Li, X.J. Wang, W. Li, Influence of a MAO + PLGA coating on biocorrosion and stress corrosion cracking behavior of a magnesium alloy in a physiological environment, Corros. Sci. 148 (2019) 134–143, https://doi.org/10.1016/j.corsci.2018.12.005.
[12] X. Qi, H. Shang, B. Ma, et al., Microstructure and wear properties of micro arc oxidation ceramic coatings, Materials 13 (4) (2020) 970, https://doi.org/10.3390/ma13040970.
[13] J. Liu, W. Yue, J. Liang, et al., Effects of evaluated temperature on tribological behaviors of micro-arc oxidated 2219 aluminum alloy and their field application, Int. J. Adv. Manuf. Technol. 96 (5) (2018) 1725–1740, https://doi.org/10.1007/s00170-017-0919-4.
[14] M. Wu, F. Jiang, Z. Tang, et al., Effect of current density on tribological properties of micro-arc oxidation ceramic film on Al-Mg-Sc alloy, Surf. Topogr. Metrol. Prop. 11 (1) (2023) 015020, https://doi.org/10.1088/2051-672x/acb9a9.
[15] G. Rapheal, S. Kumar, N. Scharnagl, et al., Effect of current density on the microstructure and corrosion properties of plasma electrolytic oxidation (PEO) coatings on AM50 Mg alloy produced in an electrolyte containing clay additives, Surf. Coat. Technol. 289 (2016) 150–164, https://doi.org/10.1016/j.surfcoat.2016.01.033.
[16] V. Ezhilselvi, J. Nithin, J.N. Balaraju, et al., The influence of current density on the morphology and corrosion properties of MAO coatings on AZ31B magnesium alloy, Surf. Coat. Technol. 288 (2016) 221–229, https://doi.org/10.1016/j.surfcoat.2016.01.040.
[17] Z. Liu, Z. Le, X. He, et al., Plasma electrolytic oxidation of tantalum in an aluminate electrolyte: Effect of cathodic polarization and frequency, Ceram. Int. 49 (22) (2023) 35042–35062, https://doi.org/10.1016/j.ceramint.2023.08.178.
[18] C.-P. Yang, X.-Z. Meng, X.-R. Li, et al., Effect of electrolyte composition on corrosion behavior and tribological performance of plasma electrolytic oxidized TC4 alloy, Trans. Nonferrous Met. Soc. China 33 (1) (2023) 141–156, https://doi.org/10.1016/S1003-6326(22)66096-5.
[19] M. Shokouhfar, C. Dehghanian, M. Montazeri, et al., Preparation of ceramic coating on Ti substrate by plasma electrolytic oxidation in different electrolytes and evaluation of its corrosion resistance: Part II, Appl. Surf. Sci. 258 (7) (2012) 2416–2423, https://doi.org/10.1016/j.apsusc.2011.10.064.
[20] L. Pezzato, L. Kostelac, L. Tonelli, et al., Effect of different types of glass powders on the corrosion and wear resistance of Peo coatings produced on 6061 aluminum alloy, Met. Mater. Int. 31 (3) (2025) 636–653, https://doi.org/10.1007/s12540-024-01786-7.
[21] L. Pezzato, S. Akbarzadeh, A.G. Settimi, et al., Corrosion and antifouling properties of copper-containing PEO coatings produced on steels, Surf. Coat. Technol. 482 (2024) 130631, https://doi.org/10.1016/j.surfcoat.2024.130631.
[22] Z. Guo, Z. Yang, Y. Chen, et al., One-step plasma electrolytic oxidation with Graphene oxide for Ultra-low porosity Corrosion-resistant TiO2 coatings, Appl. Surf. Sci. 594 (2022) 153477, https://doi.org/10.1016/j.apsusc.2022.153477.
[23] X. Qi, H. Gao, Y. He, et al., Microstructure and properties of a MAO/PA/MoS_2 composite coating formed on 6063 aluminum alloy by micro arc oxidation, Surf. Coat. Technol. 484 (2024) 130836, https://doi.org/10.1016/j.surfcoat.2024.130836.
[24] C. Yang, L. Sheng, C. Zhao, et al., Improved lubricating and corrosion resistance of MAO coatings on ZK61 Mg alloy by co-doping with graphite and nano-zirconia, J. Mater. Res. Technol. 33 (2024) 2275–2291, https://doi.org/10.1016/j.jmrt.2024.09.232.
[25] C. Zhao, M. Wen, Q. Wang, et al., Tailoring the corrosion resistance and biological performance of Mg-Zn-Y-Nd bioimplants with multiphasic, pore-sealed cerium-doped ceramic coatings via facile one-pot plasma electrolytic oxidation, J. Mater. Sci. Technol. 230 (2025) 60–79, https://doi.org/10.1016/j.jmst.2025.01.016.
[26] C. Guo, Y. Li, C. Qi, et al., Preparation and corrosion resistance characterization of MAO coating on AZ31B magnesium alloy formed in the mixed silicate and phosphate electrolytes with pectin as an additive, Surf. Coat. Technol. 476 (2024) 130209, https://doi.org/10.1016/j.surfcoat.2023.130209.
[27] C. Yang, C. Wang, X. Zhao, et al., Superhydrophobic surface on MAO-processed AZ31B alloy with zinc phosphate nanoflower arrays for excellent corrosion resistance in salt and acidic environments, Mater. Des. 239 (2024) 112769, https://doi.org/10.1016/j.matdes.2024.112769.
[28] H. Cai, X. Li, Y. Zhang, et al., A high corrosion-resistant waterborne epoxy resin coating improved by addition of multi-interface structured zinc phosphate particles, J. Mater. Res. Technol. 26 (2023) 7829–7844, https://doi.org/10.1016/j.jmrt.2023.09.109.
[29] Q. Li, J. Shang, Microstructure, wear, and corrosion behavior of an Al_2O_3-$CePO_4$-MoS_2 composite coating in-situ prepared by one-step micro arc-oxidation, Surf. Coat. Technol. (2025) 132206, https://doi.org/10.1016/j.surfcoat.2025.132206.
[30] Q. Li, J. Shang, The effects of electrolyte composition on formation and properties of micro arc oxidation coating of 6082-T6 Al alloy, Prot. Met Phys. Chem. 60 (2024) 743–757, https://doi.org/10.1134/s2070205124702022.
[31] W. Wang, C. Xin, Z. Feng, G. Li, R. Zhang, J. Hu, M. Tang, Y. Liu, W. Zhang, Ceramic coatings by microarc oxidation of Ti and Al alloys, Surf. Interfaces 33 (2022) 102260, https://doi.org/10.1016/j.surfin.2022.102260.
[32] E. Xue, J. Shang, Microstructure, performance and growth mechanism of PEO ceramic coatings on SiC/Al composite under different Na_2SiO_3 concentrations in electrolyte, Mater. Today Commun. (2025) 114102, https://doi.org/10.1016/j.mtcomm.2025.114102.
[33] Y. Li, D. Zhang, C. Qi, Y. Xue, Wang Y.L. Sun, H. Enhanced corrosion and tribocorrosion behavior of plasma electrolytic oxidized coatings on 5052 aluminum alloy with addition of pullulan to silicate electrolyte, J. Alloy. Compd. 960 (2023) 170782, https://doi.org/10.1016/j.jallcom.2023.170782.
[34] W. Li, M. Cheng, X.C. Zhang, G.K. Wei, Effects of nanoceramic particle size and content on the wear resistance of micro-arc oxidation coatings for 2A12 aluminum alloy, Heliyon 10 (2024) e38719, https://doi.org/10.1016/j.heliyon.2024.e38719.

[35] K. Zhang, S. Yu, Preparation of wear and corrosion resistant micro-arc oxidation coating on 7N01 aluminum alloy, Surf. Coat. Tech. 388 (2020) 125453, https://doi.org/10.1016/j.surfcoat.2020.125453.
[36] A.Q. Ubiedullah, A.Q. Safwan, S. Lina, V.V. Subbotina, V.V. Belozerov, O. V. Subbotin, Properties and structures of micro-arc oxide coatings on airplane aluminum alloys, J. Mech. Sci. Technol. 39 (2025) 137–142, https://doi.org/10.1007/s12206-024-1213-7.
[37] H.M. Li, S.P. Kong, Z.M. Liu, Z.X. Wang, Y.S. Geng, Hardness distribution and growth behavior of micro-arc oxide ceramic film with positive and negative pulse coordination, Nanomater. 14 (10) (2024) 842, https://doi.org/10.3390/nano14100842.
[38] X. Yang, Z. Huang, X.X. Liao, H.P. Lei, D.C. Hao, T. Zhang, B.C. Jiang, The effect of oxidation time on the organization and corrosion performance of 6061 aluminum alloy micro-arc oxidation coatings, Coatings 15 (2) (2025) 117, https://doi.org/10.1007/s11665-025-10677-w.
[39] M.J. Dai, Y.F. Cheng, Z. Wang, F. Huang, Q. Hua, J. Liu, Understanding pit initiation of pipeline steel X100 under cathodic protection potential fluctuating with various duty cycles, Corros. Commun. 12 (2023) 11–18, https://doi.org/10.1016/j.corsci.2018.08.040.
[40] Q. Li, J. Shang, Self-lubricating properties of $Al_2O_3/MoS_2/CePO_4$ composite coatings in-situ prepared by micro arc oxidation on 6082-T6 alloy, Mater. Today Commun. 40 (2024) 110137, https://doi.org/10.1016/j.mtcomm.2024.110137.
[41] A. Yoon, Z. Lee, Investigation of Oxide Phases of MoS_2: van der Waals Epitaxially Formed α-MoO_3 on MoS_2, Microsc. Microanal. 27 (S1) (2021) 646–647, https://doi.org/10.1017/S1431927621002713.
[42] Y.K. Qin, D.S. Xiong, J.L. Li, et al., Adaptive-lubricating PEO/Ag/MoS_2 multicoatinged coatings for Ti6Al4V alloy at elevated temperature, Mater. Des. 107 (2016) 311–321, https://doi.org/10.1016/j.matdes.2016.06.053.
[43] X. Qi, B. Jiang, R.G. Song, Effects of ageing treatment on corrosion behavior of 7075 aluminum alloy coated by micro arc oxidation (MAO), Corros. Sci. 199 (2022) 110164, https://doi.org/10.1016/j.corsci.2022.110164.
[44] J. Wang, S. Zhang, D. Yue, et al., Effects of calcium hydroxy-methionine on micro-arc oxidation of magnesium alloy and the underlying mechanism, J. Mater. Res. Technol. (2026), https://doi.org/10.1016/j.jmrt.2025.12.316.
[45] H. Xu, M. Ali, B. Wu, et al., Anticorrosive behavior of polyurethane coating containing hybrid attapulgite pigment, Prog. Org. Coat. 200 (2025) 109035, https://doi.org/10.1016/j.porgcoat.2024.109035.
[46] S. Yang, C. Wang, F. Li, et al., One-step in situ growth of a simple and efficient pore-sealing coating on micro-arc oxidized AZ31B magnesium alloy, J. Alloy. Compd. 909 (2022) 164710, https://doi.org/10.1016/j.jallcom.2022.164710.
[47] Q. Li, J. Shang, S. Sun, Microstructure and self-lubricating property of a novel Al_2O_3/La2P4O13/MoS_2 composite coating in-situ prepared by micro-arc oxidation, Wear (2025) 205968, https://doi.org/10.1016/j.wear.2025.205968.
[48] X. Chen, S. Tang, D. Zhang, et al., Influence of graphene on corrosion properties of micro arc oxidation coatings on 7075 aluminum alloy, Int. J. Appl. Ceram. Technol. 21 (5) (2024) 3516–3525, https://doi.org/10.1111/ijac.14767.
[49] J. Zhang, W. Dai, X. Wang, et al., Micro-arc oxidation of Al alloys: mechanism, microstructure, surface properties, and fatigue damage behavior, J. Mater. Res. Technol. 23 (2023) 4307–4333, https://doi.org/10.1016/j.jmrt.2023.02.028.
[50] C. Yang, T. Ying, A. Huang, et al., Enhancing corrosion resistance of MAO coatings on Al alloy LY12 through in situ co-doping with zinc phosphate and cerium phosphate, Corros. Commun. 17 (2025) 35–43, https://doi.org/10.1016/j.corcom.2024.10.001.
[51] C. Yang, M. Sun, T. Ying, et al., Optimization of tribological properties and corrosion resistance of MAO coatings on LY12 aluminum alloy by co-doping with graphite particles and in situ formation of zinc phosphate, Ceram. Int. 50 (22) (2024) 46018–46031, https://doi.org/10.1016/j.ceramint.2024.08.443.